



Destabilization of an Oceanic Meddy-Like Vortex: Energy Transfers and Significance of Numerical Settings

C. MÉNESGUEN AND S. LE GENTIL

Laboratoire d'Océanographie Physique et Spatiale, UMR 6523, CNRS, Ifremer, IRD, UBO, Plouzané, France

P. MARCHESIELLO

IRD/LEGOS, Toulouse, France

N. DUCOUSSO

Laboratoire d'Océanographie Physique et Spatiale, UMR 6523, CNRS, Ifremer, IRD, UBO, Plouzané, France

(Manuscript received 26 June 2017, in final form 23 March 2018)

ABSTRACT

The increase of computational capabilities led recent studies to implement very high-resolution simulations that gave access to new scale interaction processes, particularly those associated with the transfer of energy from the oceanic mesoscales to smaller scales through an interior route to dissipation, which is still underexplored. In this context, we study spindown simulations of a mesoscale interior vortex, unstable to a mixed baroclinic–barotropic instability. Even though the global energy is almost conserved, some energy is transferred down to dissipation scales during the development of instabilities. However, in our parameter regime, there is no substantial forward energy cascade sustained by unbalanced dynamics. Rather than exploring the physical parameter range, we clarify numerical discretization issues that can be detrimental to the physical solutions and our interpretation of finescale dynamics. Special care is given to determining the effective resolution of the different simulations. We improve it by a factor of 2 in our primitive equation (PE) finite-difference Coastal and Regional Ocean Community (CROCO) model by implementing a fifth-order accurate horizontal advection scheme. We also explore a range of grid aspect ratios dx/dz and find that energy spectra converge for aspect ratios that are close to N/f , the ratio of the stratification N over the Coriolis parameter f . However, convergence is not reached in the PE model when using a fourth-order centered scheme for vertical tracer advection (standard in ROMS-family codes). The scheme produces dispersion errors that trigger baroclinic instabilities and generate spurious submesoscale horizontal features. This spurious instability shows great impact on submesoscale production and energy cascade, emphasizing the significance of numerical settings in oceanic turbulence studies.

1. Context

Ocean dynamics is largely studied through the prism of numerical models. The increase of computational capabilities led recent studies to implement very high-resolution simulations with up to three decades of grid points in the three directions, giving way to new dynamical regimes. High-resolution numerical simulations provide the representation of a wide range of scales in

the study of energy spectra and fluxes. Questioning the necessary processes for dissipating the large amount of energy forced at the oceanic mesoscale, [Hua et al. \(2013\)](#) show that a quasigeostrophic (QG) model is able to produce energy fluxes in the ocean interior from mesoscale to smaller scales at a finite time in the case of a free-decay experiment.

Beyond QG dynamics, several studies have also questioned the validity of a forward energy cascade at small scale. Few of them ([Molemaker et al. 2010](#); [Nadiga 2014](#)) compare the dynamics of QG and nonhydrostatic Boussinesq (NHB) equations. [Molemaker et al. \(2010\)](#) study

Corresponding author: Claire Ménesguen, claire.menesguen@ifremer.fr

the evolution of an Eady flow in companion QG and NHB simulations. They show that in both free-decay and forced experiments, the NHB model is able to sustain small-scale secondary instabilities, which are not present in QG. They show that the interior route to dissipation in QG has only a limited duration and efficiency when dissipative scales are shifted to higher wavenumbers by increasing resolution. They conclude that balanced dynamics are limited in their capacity to efficiently dissipate energy. Unbalanced dynamics are required for the interior route to dissipation. Following the same idea, [Nadiga \(2014\)](#) broadens the concept to an unstable flow, free-decaying from a Phillips-type baroclinic instability simulated with a pseudospectral model in a domain with size $100\text{ km} \times 100\text{ km} \times 5000\text{ m}$ and grid resolution $dx < 0.1\text{ km}$. He pays particular attention to the grid aspect ratio dx/dz , which is scaled on the ratio of the stratification N over the Coriolis parameter f in order to avoid spurious gravity wave activity ([Lindzen and Fox-Rabinovitz 1989](#); [Snyder et al. 1993](#)). As in [Molemaker et al. \(2010\)](#), [Nadiga \(2014\)](#) highlights a substantial forward energy cascade. In his configuration, the forward cascade occurs for scales smaller than 5 km with increasing amplitude for higher Rossby number values. [Brüggemann and Eden \(2015\)](#) also revisit an Eady flow experiment applied to an oceanic surface layer configuration (domain size is $\sim 1.4\text{ km} \times \sim 1.4\text{ km} \times 200\text{ m}$) with a primitive equation (PE) model. They show an increased forward cascade with decreasing Richardson number (which correspond in their case to decreasing N/f ratio) at scales smaller than 700 m .

Another set of experiments ([Pouquet and Marino 2013](#); [Marino et al. 2015](#)) address the question of relative amplitudes of direct and inverse energy fluxes. The authors use simulations of an idealized ocean basin using a pseudospectral NHB model on a cubic domain $[(4500\text{ m})^3]$, up to 2048^3 grid points]. Their grid aspect ratio dx/dz is set to 1 in order to properly represent nonhydrostatic dynamics. They highlight a forward energy cascade generated by a stochastic forcing at scales smaller than the forcing scale (around 450 m in their oceanic application). [Pouquet and Marino \(2013\)](#) show an increase of the forward cascade with higher Rossby and Reynolds numbers, while [Marino et al. \(2015\)](#) show a direct flux increase with higher N/f ratio. However, as noted by [Capet et al. \(2016\)](#), stratification remains weak in their experiments ($N/f \lesssim 10$, which is a realistic value in the ocean bottom but not in the surface layers).

In these oceanic applications, substantial forward energy cascade is generally found at very small scales ($< 700\text{ m}$), except in [Nadiga \(2014\)](#) where a forward cascade appears at scales smaller than 5 km . In an oceanic variant of the Charney baroclinic instability experiment,

[Capet et al. \(2016\)](#) do not reveal any substantial forward cascade, even though a small positive flux is found for scales smaller than 20 km (the domain size is $512\text{ km} \times 2040\text{ km} \times 4000\text{ m}$). They use a finite-difference PE model with horizontal resolution of $dx = 1\text{ km}$. Following [Soufflet et al. \(2016\)](#), we estimate an effective resolution of $\sim 10\text{ km}$ in their simulation. In this case, we may question the model capability to solve a forward energy cascade for scales smaller than 20 km . However, another question is raised from comparing the different studies: a substantial forward cascade is found in experiments when the ratio N/f is less than or equal to 10. The only experiments with high N/f ratio (between 30 and 45) are found in [Capet et al. \(2016\)](#), which better represents the range of oceanic values.

Our study addresses the problem of an interior instability (close to a Phillips baroclinic instability) using two different formalisms: a pseudospectral QG model and a finite-difference PE model. Our N/f ratio is 28, which accounts for North Atlantic dynamics near the Mediterranean outflow, from the surface to 2400-m depth. Our setup and tools are similar to that of [Capet et al. \(2016\)](#), except that we do not focus on surface-intensified dynamics. Rather, we investigate a weakly baroclinically unstable interior vortex in the regime represented by a low Rossby number and relatively large N/f ratio (resembling an idealized meddy, i.e., Mediterranean water eddy). We will show that this regime does not lead to significant forward energy cascade. In addition, the study will emphasize the importance of numerical settings in finite-difference PE models for properly representing submesoscale energy transfers. The question of the influence of N/f or other physical parameters, such as the Rossby number, is the topic of another study.

The paper is organized as follows. The model setup and initial conditions are presented in [section 2](#). In [section 3](#), we describe the nonlinear evolution of vortex destabilization and its propensity for producing layer structures. In [section 4](#), we discuss the meaning and validity of a positive flux in kinetic and available potential energies in both QG and PE formalisms for our spindown experiment. [Section 5](#) addresses the impact of numerical settings when discussing energy transfers and spectral slopes in a turbulent flow. Our method is to compare two companion experiments, one in a QG framework with a pseudospectral model and the other in a PE framework with a finite-difference model.

2. Formulation and numerical setup

In this paper, we perform highly idealized simulations of the dynamics of an anticyclonic eddy in a rotating stratified flow on an f plane, using quasigeostrophic

and primitive equations. The numerical simulations are spindown experiments.

a. QG model

The QG equations are implemented as in Pedlosky (1996):

$$\frac{\partial Q}{\partial t} + J(\psi, Q) = \nu \nabla^2 \psi, \quad (1)$$

where ψ is the streamfunction, $J(\dots)$ is the horizontal Jacobian operator, ν is hyperviscosity required to dissipate potential enstrophy at the smallest scales in the numerical simulations, and Q is the QG potential vorticity (PV) defined as follows:

$$Q \equiv f + \nabla^2 \psi + \partial_z \left(\frac{f^2}{N^2} \partial_z \psi \right), \quad (2)$$

where $\nabla \equiv (\partial/\partial x, \partial/\partial y)$, z is the vertical coordinate, f is the Coriolis parameter, and N is the background Brunt–Väisälä frequency. By the thermal wind equation, we have buoyancy $b = f \partial_z \psi$, and for a constant $N = N_0$, we obtain

$$Q/f - 1 = \zeta/f + \partial_z b/N_0^2. \quad (3)$$

The numerical code is the pseudospectral 3D QG version of Hua and Haidvogel (1986), which is parallelized on the vertical. The code is pseudospectral on the horizontal and modal on the vertical [see appendix in Hua et al. (2013) for more details]. Temporal discretization is performed with a leapfrog scheme stabilized by occasional insertion of a trapezoidal correction (predictor–corrector scheme).

b. PE model

The PE model code is the Coastal and Regional Ocean Community (CROCO) model, a version of the Regional Oceanic Modeling System (ROMS) designed for simulating high-resolution offshore and nearshore dynamics (Shchepetkin and McWilliams 2005; Debreu et al. 2012; Soufflet et al. 2016). It is a split-explicit, free-surface, and terrain-following vertical coordinate oceanic model discretized on a C grid. The time-stepping algorithm is third-order accurate for the integration of advective terms and second-order accurate for internal gravity waves. It is a leapfrog Adams–Moulton predictor–corrector scheme (LF-AM3) complemented with a forward–backward (FB) feedback to extend the range of stability for internal gravity waves. The barotropic mode is integrated with a generalized FB scheme (AB3-AM4; a three-level Adams–Bashforth step for free-surface and a four-level Adams–Moulton step for velocities), which is third-order accurate. Besides inheriting

high-order time-stepping methods from ROMS, CROCO has innovative algorithms for temporal and spatial discretization and additional capabilities for oceanic applications (e.g., two-way nesting; Debreu et al. 2012). For mode coupling, a more selective filtering of the barotropic mode is used (dissipation added to the barotropic time-stepping scheme, rather than ROMS averaging filters; Demange et al. 2014), which is required for controlling aliasing and splitting errors in split-explicit ocean models. Horizontal advection terms for tracers and momentum are discretized with fifth-order (UP5) rather than third-order (UP3) upwind advection schemes [e.g., Durran (2010) for details on upwind advection schemes]. No horizontal viscosity or diffusivity is added since upwind schemes have a dissipative leading-order error and are optimally built for damping dispersive (phase) errors (Soufflet et al. 2016). On the vertical, advection is discretized with fourth-order centered parabolic spline reconstruction (Splines scheme; Shchepetkin 2015). Small background diffusion and dissipation are prescribed for wave breaking with a Laplacian operator and coefficients set, respectively, to 10^{-6} and $10^{-5} \text{ m}^2 \text{ s}^{-1}$. In addition, diffusion and dissipation can locally be enhanced for turbulent mixing depending on the local Richardson number and for occurrence of static instability as described in Large et al. (1994). However, in simulations presented in this paper, the dynamical regime never activates such locally enhanced dissipation coefficients. This numerical setting and its impact on energy transfer at small scale are discussed in section 5.

The primitive equations in CROCO are the usual set of nonlinear differential equations that consist of three main sets of equations—momentum, density, and continuity—with hydrostatic and Boussinesq approximations and Reynolds decomposition. The primitive equations conserve the Ertel PV PV_E (e.g., Bartello 1995; Nadiga 2014) given by

$$\begin{aligned} PV_E &= (\omega + f\mathbf{z})(N_0^2 \mathbf{z} + \nabla b)/N_0^2 \\ &= f + (\zeta + f/N_0^2 \partial_z b) + (\omega \nabla b)/N_0^2, \end{aligned} \quad (4)$$

where ω is the relative vorticity, ζ its vertical component, N_0 is a constant Brunt–Väisälä frequency, \mathbf{z} is the vertical unit vector, and b is the buoyancy field, excluding the linear background stratification:

$$PV_E/f - 1 = \zeta/f + \partial_z b/N_0^2 + (\omega \nabla b)/fN_0^2 \quad (5)$$

c. Vortex initialization in the QG model

For the QG simulation, the initial base state is given by an initial streamfunction:

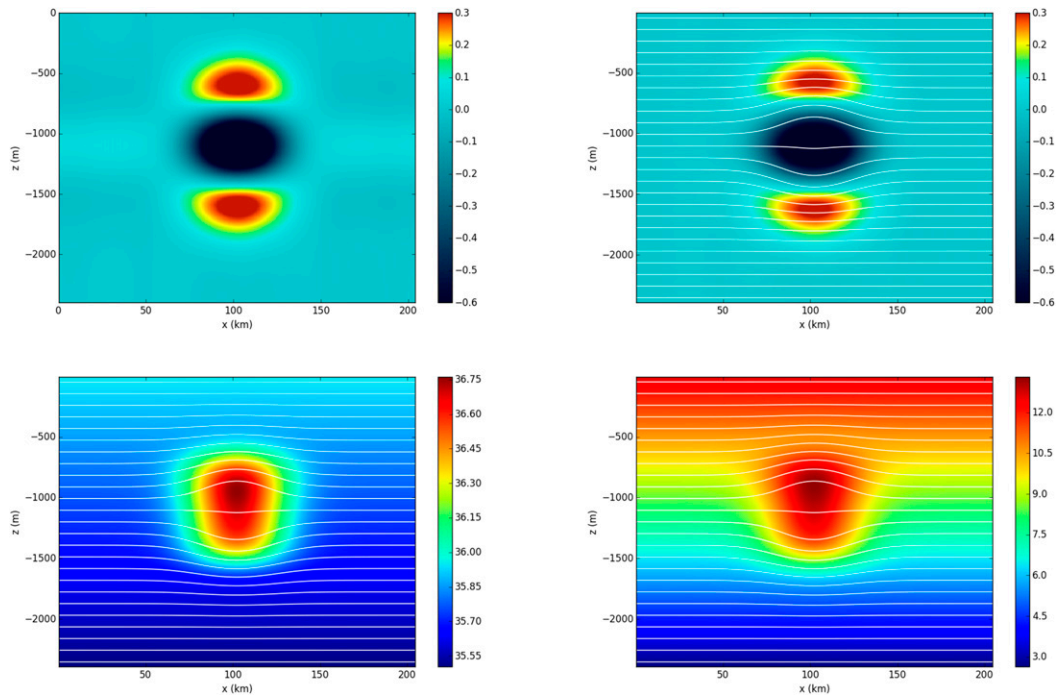


FIG. 1. Meddy initialization. (top) Vertical sections across the vortex axis showing (left) $(Q/f - 1)$ and (right) $(PV_E/f - 1)$ for the QG and PE simulations; (bottom) same sections in the PE simulation, for initial fields of (left) salinity and (right) temperature.

$$\psi_0 = -\frac{Ro}{4} fL^2 \exp\left[-\left(\frac{x-x_0}{L}\right)^2 - \left(\frac{y-y_0}{L}\right)^2 - \left(\frac{z-z_0}{H}\right)^2\right]. \quad (6)$$

Constant values are chosen to represent meddy dynamics with Coriolis parameter $f = 8 \times 10^{-5} \text{ s}^{-1}$ and $N_0 = 2.23 \times 10^{-3} \text{ s}^{-1}$. Length scales L and H are, respectively, 28 km and 390 m. In most of our simulations, the strength of the anticyclonic vortex is set by $Ro = -0.3$ (simulations with $Ro = -0.16$ show no dramatic changes). The Burger number is defined as $Bu = (N_0 H / fL)^2$. For most of our simulations, $Bu = 0.15$ (the other group of simulations is computed with $Bu = 0.2$). In every case, the vortex is slightly unstable to a mixed baroclinic–barotropic instability (Nguyen et al. 2012; Yim et al. 2016; Storer et al. 2018).

The domain is a basin whose size is $Lx = Ly = 204.8 \text{ km}$ and $Lz = 2400 \text{ m}$. For the highest resolutions ($512^2 \times 480$ grid points), we have $dx = 400 \text{ m}$ and $dz = 5 \text{ m}$.

Small random perturbations are added in all simulations. Particular care is given to maintain exactly the same perturbations at different resolutions. The initiation of instability is highly dependent on the perturbation, even though its dynamics are robust.

The nondimensional QG PV anomaly $(Q/f - 1)$ due to the vortex is plotted in Fig. 1a. The radial gradient of Q changes sign over the domain, confirming the conditions for baroclinic and barotropic instabilities.

d. Vortex initialization in the PE model

In the PE simulations, the same vortex is initialized with a corresponding density field. The velocity field is obtained via the cyclogeostrophic equilibrium. This prevents the emission of fast waves emitted during a primary adjustment but also produces a small difference in the initial energy settings of companion QG and PE simulations.

The stratification is calculated from temperature and salinity via a linear equation of state:

$$\rho = \rho_0 - \alpha(T - T_0) + \beta(S - S_0), \quad (7)$$

with $T_0 = 12^\circ\text{C}$, $S_0 = 36.6 \text{ psu}$, $\alpha = 0.16 \text{ kg m}^{-3} \text{ }^\circ\text{C}^{-1}$, and $\beta = 0.8 \text{ kg m}^{-3} \text{ psu}^{-1}$. Because our experiments simulate a meddy, we added meddy-like temperature and salinity anomalies that are compensated in the density field. The vortex is a warm and salty lens (Fig. 1, bottom row). However, in order to prevent the occurrence of double diffusion, temperature and salinity are given the same diffusivity (as described in section 2b).

For dynamics, the same characteristic meddy-like values of QG simulations are chosen for the PE model: $f = 8 \times 10^{-5} \text{ s}^{-1}$, $N_0 = 2.23 \times 10^{-3} \text{ s}^{-1}$, $g = 9.8 \text{ m s}^{-2}$, and $\rho_0 = 1027 \text{ kg m}^{-3}$. As in QG simulations, the characteristic lengths of the vortex are $L = 28 \text{ km}$ and $H = 390 \text{ m}$ and the domain size is $L_x = L_y = 204.8 \text{ km}$ and $L_z = 2400 \text{ m}$. For most of the simulations, the strength of the vortex is set by $\text{Ro} = -0.3$.

For the highest resolutions ($1024^2 \times 480$ grid points), the discretization is $dx = 200 \text{ m}$ on the horizontal (twice as fine as its QG companion; see below) and $dz = 5 \text{ m}$ on the vertical.

Small random perturbations are added in all simulations. Particular care is given here also to maintain exactly the same perturbations at different resolutions and to have the same perturbations as in the companion QG simulations.

The nondimensionalized Ertel PV anomaly ($\text{PV}_E/f - 1$) due to the vortex is plotted in Fig. 1b. This field is very close to the initial QG PV anomaly of the companion QG simulation (Fig. 1a).

3. Spindown and layering formation

a. Vortex destabilization

As shown in previous papers (Nguyen et al. 2012; Hua et al. 2013; Yim et al. 2016; Storer et al. 2018), the vortex is unstable to a mixed baroclinic–barotropic instability. For our parameter values ($\text{Ro} = 0.1\text{--}0.3$, $\text{Bu} = 0.15\text{--}0.2$), an azimuthal mode 2 is dominant, forming spiral arms winding around the vortex as highlighted in seismic observation of meddies (Song et al. 2011; Ménesguen et al. 2012).

Figure 2 shows a middepth section of the vortex PV in the QG and PE simulations for different time steps. The vortex evolution in the QG framework can be compared with Fig. 7 of Hua et al. (2013). Similar evolution is observed with the winding of spiral arms around the vortex and, eventually, the creation of small vortices. In the PE simulation, the same instability occurs with the growth of an azimuthal mode 2 (right column of Fig. 2) winding spiral arms around the vortex.

b. Energetics: Global budgets

Thereafter, our spindown experiment focuses on the mixed baroclinic–barotropic instability that is apparent in global energy budgets.

In the QG formulation, kinetic energy (KE) and available potential energy (APE) are defined as follows:

$$\text{KE} \equiv \frac{1}{2} \|\nabla\psi\|^2, \quad \text{and} \quad (8)$$

$$\text{APE} \equiv \frac{1}{2} \frac{f^2}{N_0^2} (\partial_z \psi)^2 = \frac{1}{2} \frac{b^2}{N_0^2}. \quad (9)$$

For the PE formulation, we choose to adopt the QG definition of APE:

$$\text{KE} \equiv \frac{1}{2} (u^2 + v^2), \quad \text{and} \quad (10)$$

$$\text{APE} \equiv \frac{1}{2} \frac{g\rho'^2}{\rho_0 |\partial_z \rho'|}, \quad (11)$$

with the reference density profile ρ^r as the horizontal average of the 3D density field, which has been sorted in a monotonic function and the density perturbation defined as $\rho' = \rho - \rho^r$.

Total budgets of KE, APE, and total energy were evaluated and are shown in Fig. 3. After 50 days, as expected for baroclinic instability, there is loss of APE in favor of KE. Note, however, that during our experiments, the total energy is globally almost conserved and global dissipation during spindown remains weak.

c. Layering formation

Evidence of persistent layering, with vertical stacking of sharp variations in temperature, has been more clearly revealed at the vertical and lateral periphery of energetic oceanic vortices through seismic imaging of the water column (Biescas et al. 2008; Ménesguen et al. 2012). Hua et al. (2013) argued that this layering is reproduced by the destabilization of an unstable vortex in QG dynamics. They showed, in their Fig. 8, vertical sections of vortex stretching, which is a proxy for vertical temperature gradients in simulations where temperature is the only component of the density field. Their figure clearly shows a layering pattern surrounding a vortex. The same features are reproduced here in the left column of Fig. 4.

However, Meunier et al. (2015) point out the importance of isopycnal stirring in the process of creating noticeable layering in the temperature field, as observed in seismic imaging. They show that primary vortex instabilities can produce small-scale perturbations around the vortex. These perturbations are then simply isopycnally wrapped around the vortex, stirred by the velocity field. Using a PE model, they show by this process how an unstable meddy-like vortex with temperature and salinity anomalies can create layers around the vortex in the temperature (or salinity) anomaly field.

For comparison with Hua et al. (2013) and layering observed in the QG simulation, we show vertical

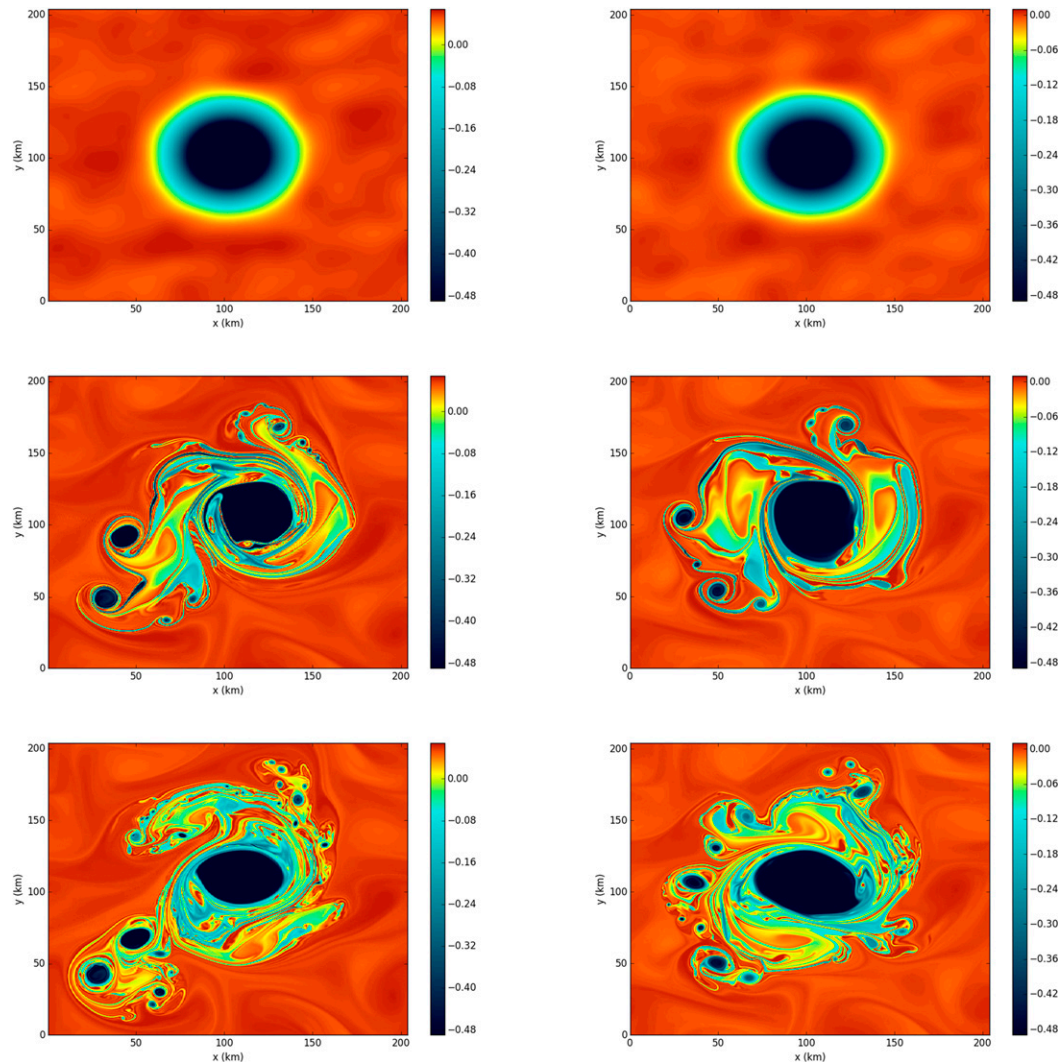


FIG. 2. Horizontal middepth section of (left) $(Q/f - 1)$ for the QG simulation and (right) $(PV_{Elf} - 1)$ for the PE simulation at days 0, 120, and 148.

sections of vortex stretching (the vertical gradient of ρ_z) in Fig. 4 (right column) in the PE simulation. Layers are well reproduced. Now, the observed quantity in seismic

data is rather similar to a vertical gradient of temperature anomalies (Nandi et al. 2004). Therefore, it is useful to also present this field T'_z in Fig. 5. Even though

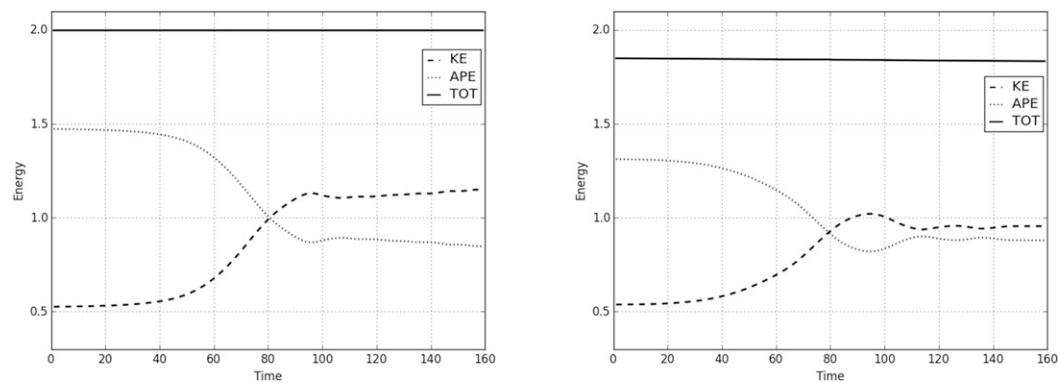


FIG. 3. Time evolution of kinetic (dashed line), potential (dotted line), and total (solid line) energy for the (left) QG and (right) PE simulations. Note that the total energy is almost constant as dissipation is weak.

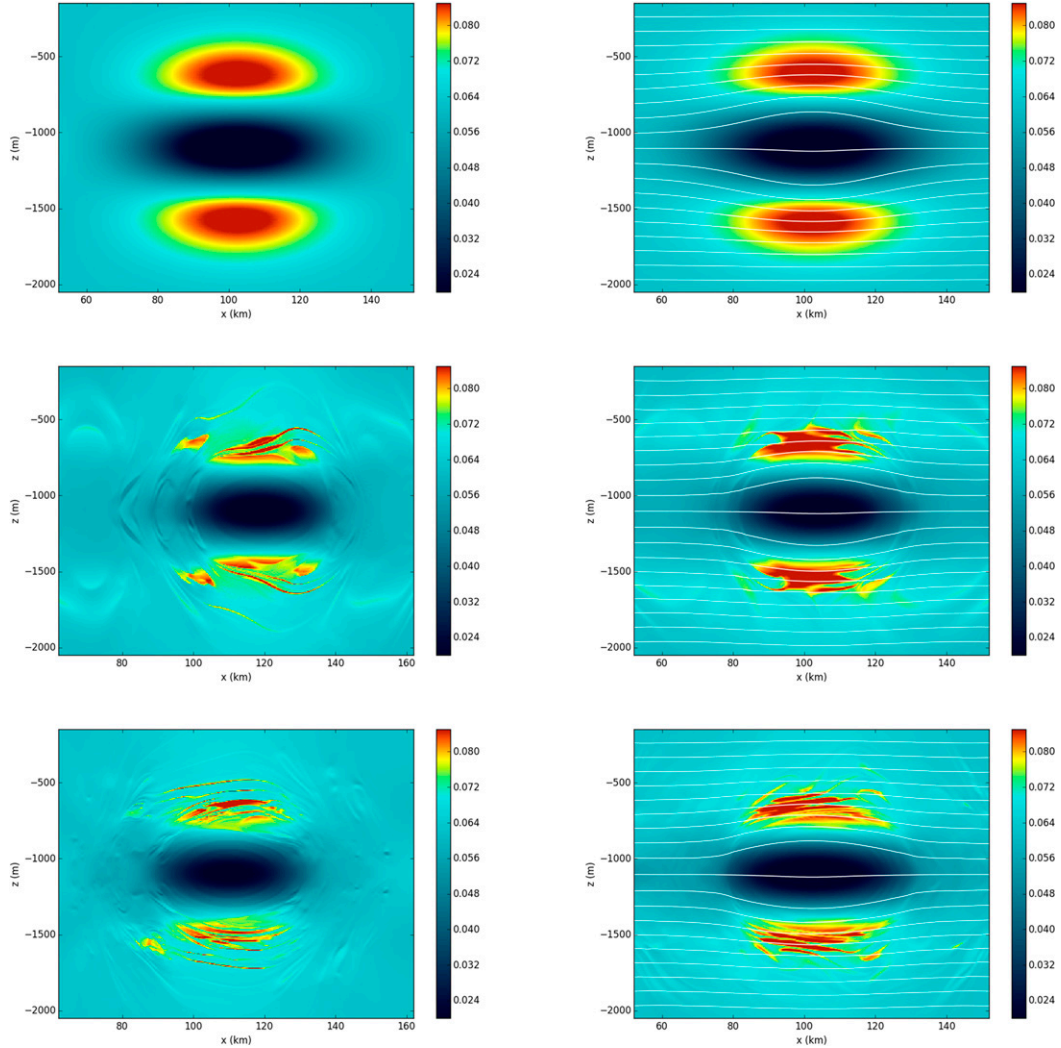


FIG. 4. Vertical sections of (left) vortex stretching ($N_0^2/f + \psi_{zz}$) for the QG simulation and (right) $-gp_z/f\rho_0$ for the PE simulation at days 0, 120, and 148.

layering in the vortex stretching field is relatively smooth in the PE simulation, the simulated vertical gradient of temperature anomalies fairly resembles the layering observed in seismic imaging. In our case, layering in the temperature field is due to a mix of stirring and other processes affecting the PV field.

4. Quantification of small-scale production in the spectral space

Here, we focus on the quantification of small-scale production, using a spectral formalism. Hua et al. (2013) show, from a similar spindown experiment, that positive flux at small scale can be expected in a QG framework. We revisit this result and extend it to the PE framework.

a. KE and APE equations in the QG formalism

From the quasigeostrophic equations of motion,

$$\frac{\partial \nabla^2 \psi}{\partial t} = -J(\psi, \nabla^2 \psi) + f \frac{\partial}{\partial z} w + \nu \nabla^{12} \psi, \quad \text{and} \quad (12)$$

$$\frac{\partial b}{\partial t} = -J(\psi, b) - N^2 w, \quad (13)$$

where w is the vertical velocity, which is obtained through the quasigeostrophic ω equation (Hoskins et al. 1978).

In the spectral space, the levelwise kinetic and available potential energy budgets are computed at a given level z as a function of horizontal wavenumber space k_h [$k_h \equiv (k^2 + l^2)^{1/2}$, where k, l are the zonal and meridional wavenumbers]:

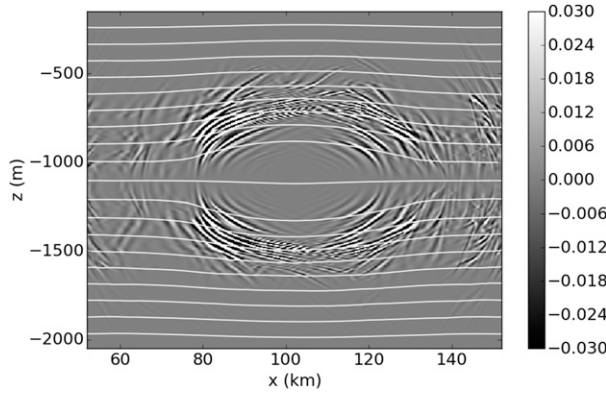


FIG. 5. Vertical sections of vertical gradient of temperature anomaly at day 148 for the PE simulations. For comparison with seismic data, the anomaly is defined as the subtraction of a Butterworth low-pass-filtered field to the global temperature, removing scales higher than 500 m.

$$\frac{\partial \widehat{\text{KE}}}{\partial t} = \text{Re} \left[\hat{\psi}^* J(\widehat{\psi}, \nabla^2 \widehat{\psi}) - f \frac{\partial(\hat{\psi}^* \hat{w})}{\partial z} + \hat{w} \hat{b}^* - \nu \hat{\psi}^* \nabla^{12} \widehat{\psi} \right], \quad \text{and} \quad (14)$$

$$\frac{\partial \widehat{\text{APE}}}{\partial t} = \text{Re}[-N^{-2} \hat{b}^* J(\widehat{\psi}, \widehat{b}) - \hat{w} \hat{b}^*]. \quad (15)$$

Here, $\widehat{\cdot}$ denotes the horizontal spectral transform, the asterisk stands for the complex conjugate, and Re is the real part.

Levelwise horizontal spectral fluxes $\Pi(k_h, z)$ of, respectively, potential and kinetic energy are evaluated as follows (see, e.g., Frisch 1995): $\Pi(k_h, z) = \int_{k_h}^{\infty} T(k_h, z) dk_h$, where $T(k_h, z)$ corresponds to the right-hand side terms in Eqs. (14) and (15).¹ The entire domain energy fluxes $\int \Pi(k_h, z) dz$ are plotted in Fig. 6a in variance-preserving form, such that fluxes are multiplied by the horizontal wavenumber. As in Hua et al. (2013), we obtain substantial positive fluxes toward small scales in the submesoscale range (2–10 km).

b. KE and APE equations in the primitive equations

From the primitive equations of motion, we obtain levelwise kinetic and available potential energy budgets in the spectral space:

$$\frac{\partial \widehat{\text{KE}}}{\partial t} = \text{Re} \left[-\widehat{\mathbf{u}}_H^* \cdot (\widehat{\mathbf{u}}_H \cdot \widehat{\nabla}_H)_{C6} \widehat{\mathbf{u}}_H - \widehat{\mathbf{u}}_H^* \cdot w \frac{\partial \widehat{\mathbf{u}}_H}{\partial z} - \frac{1}{\rho_0} \widehat{\mathbf{u}}_H^* \cdot \widehat{\nabla}_H \widehat{p} + \widehat{\mathbf{u}}_H^* \cdot \widehat{\mathbf{D}}_{\text{UP5}} + \widehat{\mathbf{u}}_H^* \cdot \frac{\partial}{\partial z} \nu \frac{\partial}{\partial z} \widehat{\mathbf{u}}_H \right], \quad \text{and} \quad (16)$$

$$\frac{\partial \widehat{\text{APE}}}{\partial t} = \frac{g}{\rho_0 |\partial_z \rho^r|} \text{Re} \left[-\widehat{\rho}^* (\widehat{\mathbf{u}}_H \cdot \widehat{\nabla}_H)_{C6} \widehat{\rho} - \widehat{\rho}^* w \frac{\partial \widehat{\rho}}{\partial z} + \widehat{\rho}^* \widehat{D}_{\text{UP5}} + \widehat{\rho}^* \frac{\partial}{\partial z} \kappa_v \frac{\partial}{\partial z} \widehat{\rho} \right], \quad (17)$$

where \mathbf{u}_H is the horizontal part of the velocity field and w its vertical component, $(\widehat{\mathbf{u}}_H \cdot \widehat{\nabla}_H)_{C6}$ is the advection due to an order 6 centered scheme, D_{UP5} is the dissipation part of the upwind scheme, ν_v is the vertical dissipation coefficient and κ_v is the vertical diffusion coefficient.

Despite weaker submesoscale fluxes compared with those in the QG companion simulation, we do observe in Fig. 6b positive fluxes in the submesoscale range (2–10 km). This result is thus robust enough to be found in different formalisms, with different code architectures. However, we may question the dependence of this forward cascade on physical parameters. In Storer et al. (2018), the dependence of small-scale production on the Burger number in a QG regime is illustrated in their Fig. 13. Small-scale production is higher for their smallest Burger number. The dependence in Rossby number is also relevant and will be the topic of another study.

c. Time dependence

In a spindown simulation, time is a critical parameter. Instead of averaging fluxes, as presented in Fig. 6 (average between 80 and 120 days), we now present their time evolution in Fig. 7.

We find the following for both models: (i) the instability with its baroclinic component (Yim et al. 2016; Storer et al. 2018) transfers APE to KE (between ~ 40

¹ Note that the kinetic energy and the available potential energy are not conserved separately. The computed fluxes of potential and kinetic energy include sources and sinks (that quantify the exchange between APE and KE at a given wavenumber; and viscous terms). Sources and sinks in these equations vanish only when the total flux is computed (except for the viscous term). However, we broaden the use of the word “flux” for these quantities.

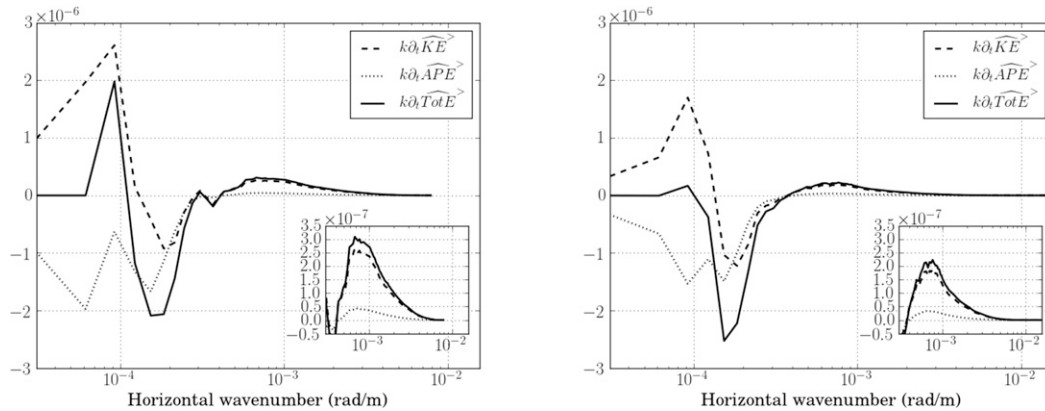


FIG. 6. Energy fluxes (m s^{-3}) integrated over the whole domain, averaged between 80 and 120 days and plotted in variance preserving form for (left) the QG simulation and (right) its companion PE simulation. In the inset the vertical scale is refined in the wavenumber range of small scales to better appreciate the positive flux.

and ~ 90 days) while conserving total energy (the column corresponding to the lower horizontal wavenumber is equivalent to the time derivative of quantities shown in Fig. 3 presenting energy budgets over the whole domain), and (ii) mesoscale (30–60 km) energy fluxes oscillate in time and do not converge. This is due to the rotation of the vortex, which is deformed by a mode 2 into an oval shape in a horizontal plane. In the time lapse of the experiment, the vortex is not yet reaxisymmetrized. Therefore, fluxes for this scale range are not relevant to time-averaged values in Fig. 6.

In terms of spectral energy distribution, Fig. 8 shows the time evolution of the spectral slope. The mixed baroclinic–barotropic instability fills the energy spectra in the small-scale range until a slope between -3 and $-5/3$ [i.e., between a typical QG turbulence spectrum and a spectrum found in Hua et al. (2013) and explained by geometrical arguments]. Because dissipation is weak, the spectral slope remains constant after the instability development (after ~ 120 days).

In the given parameter regime, chosen for its relevance to a typical (rather old) oceanic meddy, PE simulations sustain a positive flux at small scale that does not last longer than in QG dynamics. Indeed, PE simulations do not yield small-scale secondary instabilities that would sustain an efficient forward energy flux (Molemaker et al. 2010; Nadiga 2014). Contrary to our simulations, in situ observations show vertical density profiles forming staircases above or below meddies, which corresponds to mixing events (e.g., Armi et al. 1989). Note that staircase structures are not necessarily well sampled by the seismic technique, depending on its source frequency, and are not the only feature seen by seismic observations, which reveal vertical gradients of temperature anomalies. Layering seen by seismic data may simply result from stirring

effects (Meunier et al. 2015). In any case, mixing events are observed around meddies and often associated with double-diffusive effects, although other submesoscale instability processes may be at work. It is not clear to us whether PE simulations miss these events because 1) we did not use any double-diffusive parameterization, 2) the chosen parameter regime is close to QG dynamics and unfavorable to unbalanced dynamics, and 3) the resolution is still too coarse to solve submesoscale processes. However, there is clearly a sensitivity of our solutions to the choice of numerical schemes. Therefore, in the following, we focus on the definition of effective resolution and discuss the impact of numerical setting on model solutions.

5. On the role of numerical settings

a. Impact of resolution and numerical dissipation

1) EFFECTIVE HORIZONTAL RESOLUTION

Figure 9 shows the right-hand side terms of KE Eqs. (14) and (16) for QG and PE simulations at their highest resolutions ($dx = 400$ and 200 m, respectively), averaged between 80 and 120 days (as in Fig. 6). The same calculation for right-hand side terms of APE Eqs. (15) and (17) is illustrated in Fig. 10.

In the left column of Fig. 9, explicit dissipation in QG simulations (magenta curve) becomes important at small scale with a classical bell shape. Maximum dissipation occurs at $k_h = 5 \times 10^{-3}$ cpm. It balances the advection term at the end of the spectrum and does not affect the positive flux between 10 and 2 km. The right columns of Figs. 9 and 10 present the same spectral calculation for companion PE simulations. Here again, the implicit damping provided by the UP5 advection

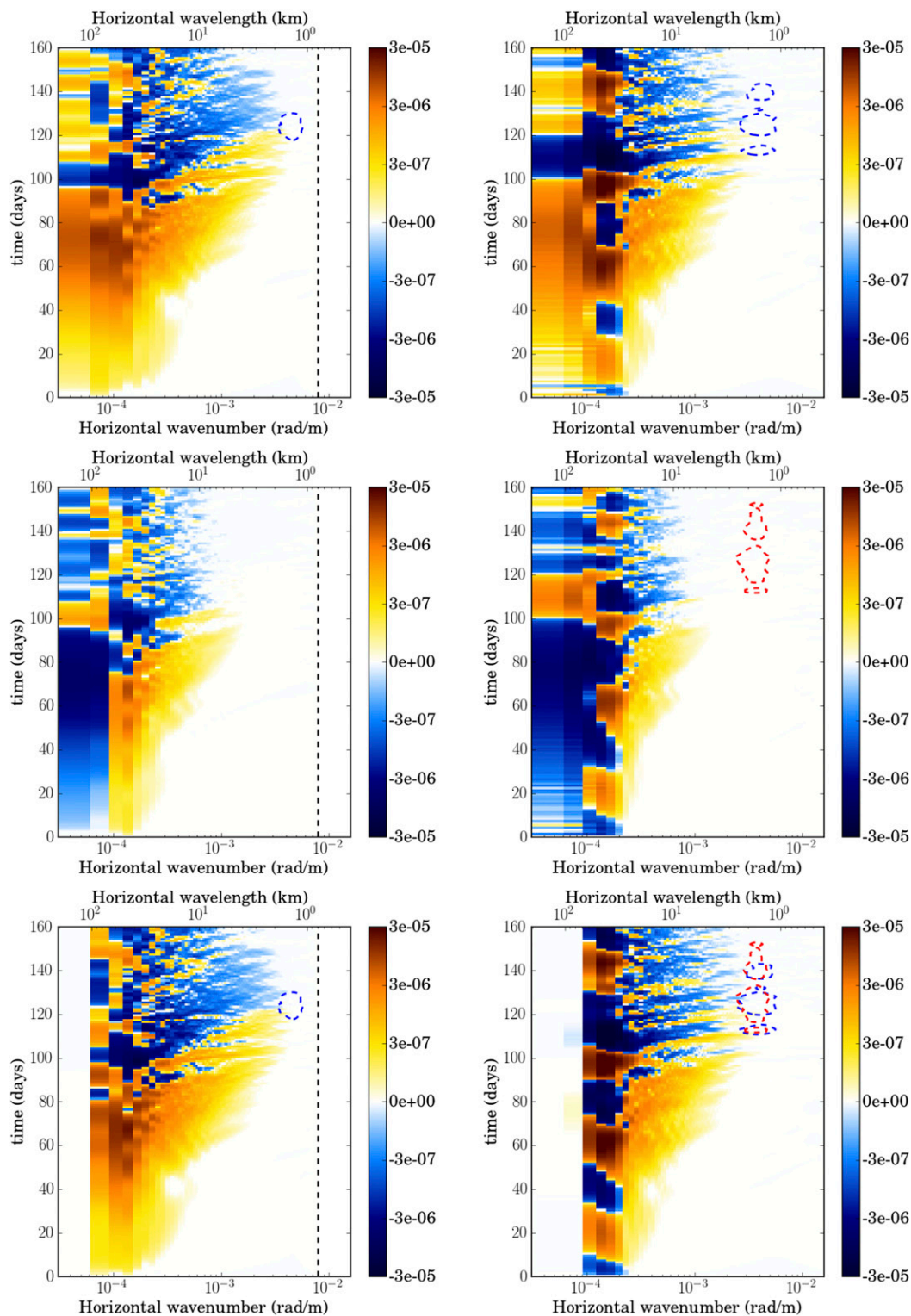


FIG. 7. Time evolution of spectral fluxes (m s^{-3}) for the (left) QG and (right) PE simulations. Maximum KE dissipation is contoured in blue dashed line (top) in the KE flux and (bottom) in the total energy flux subplots. Maximum dissipation is contoured in red dashed line (middle) in the APE flux and in the total energy flux subplots in the PE simulation. The resolution of the QG simulation is denoted by a vertical black dashed line. Note that despite the different horizontal grid resolution for the two simulations, the dissipation maxima are located at a similar length scale. These QG and PE simulations have similar effective resolution.

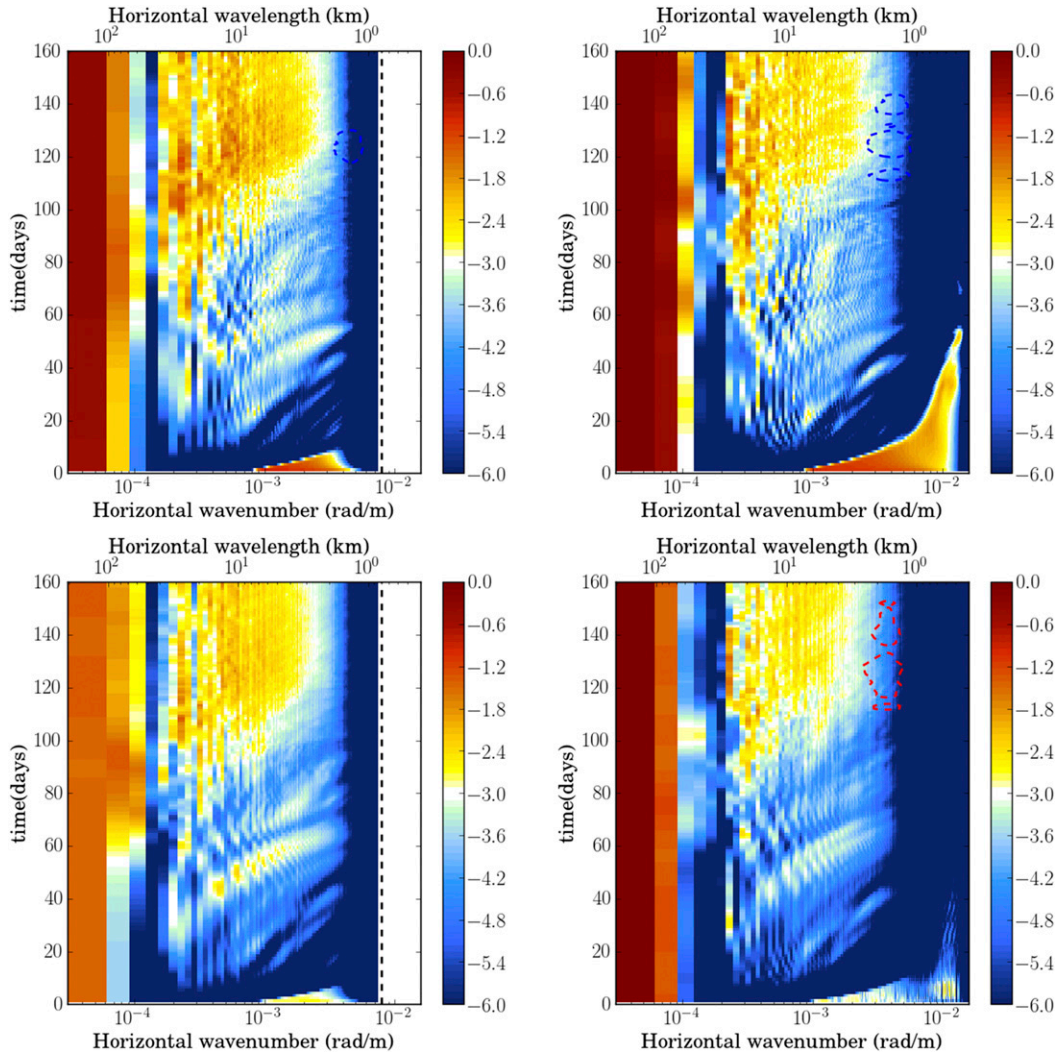


FIG. 8. Time evolution of spectral slopes for the (left) QG and (right) PE simulations: (top) $\partial \log_{10}(\widehat{KE}) / \partial \log_{10}(k)$ and (bottom) $\partial \log_{10}(\widehat{APE}) / \partial \log_{10}(k)$. Maximum KE dissipation is contoured in blue dashed line and maximum APE dissipation is contoured in red dashed line. The resolution of the QG simulation is denoted by a vertical black dashed line.

scheme for momentum/tracers becomes a major player only at the very end of the spectra. The maximum is at $k_h = 4 \times 10^{-3}$ cpm. Therefore, the positive flux and small-scale production between 10 and 2 km are within an inertial range, free of dissipation.

The end of the spectra, where advection is balanced by dissipation, defines the effective resolution (Marchesiello et al. 2011; Soufflet et al. 2016). In the QG spectral code, explicit dissipation sets $dx_{\text{eff}} \sim 3dx$ ($dx_{\text{eff}} = 1.3$ km for the highest resolution performed in this paper). In the PE code, dissipation given by UP5 advection scheme sets $dx_{\text{eff}} \sim 8dx$ ($dx_{\text{eff}} = 1.6$ km for the highest resolution). As expected, dissipation in the PE simulation has a broader spectrum because the order-6 dissipation operator within

UP5 is obviously less scale selective than the order-12 operator used in the QG model.

It is worth commenting on the difference of numerical treatment of dissipation operators between the QG and PE models. At order n , hyper-dissipation in the pseudo-spectral QG model should vary as k^n . This is also true for the finite-difference PE model except near the grid scale where the damping factor flattens as a result of truncation errors (see Soufflet et al. 2016). The model's effective resolution is not set by this small error on the dissipation operator but by the dissipation operator itself. In this sense, comparing the order of dissipation operators in QG and PE models is relevant to a comparison of effective resolution.

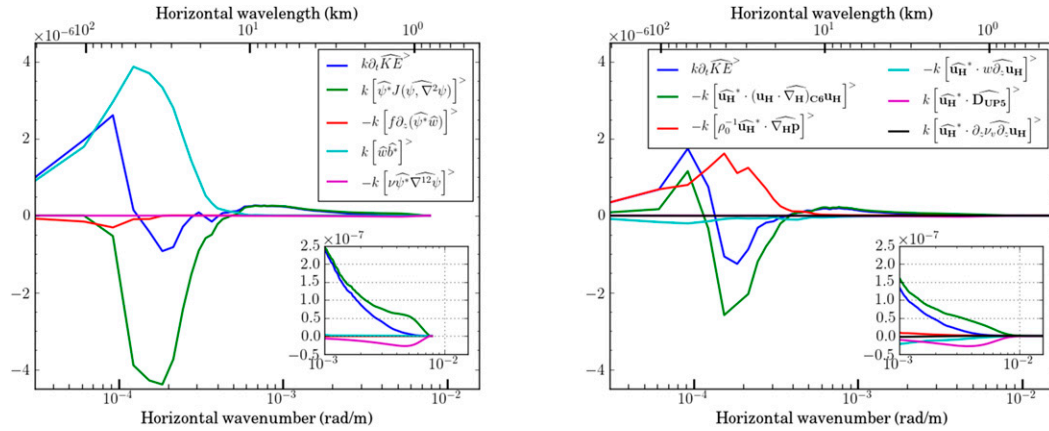


FIG. 9. KE budget (m s^{-3}) averaged between 80 and 120 days for (left) QG and (right) PE simulations. Terms are detailed in Eqs. (14) and (16). Note that dissipation is only significant at small scale, beyond the scale range of significant positive spectral flux. The effective resolution is fine enough that an inertial range can develop.

The effective resolution of the QG model is more than twice that of the PE model. Because a fair comparison between QG and PE simulations requires equivalent dissipation scales (i.e., effective resolution), we choose to compare QG simulations with companion PE simulations that have twice as fine horizontal grid resolution. Figures 11 and 12 show KE and APE spectra and dissipation terms at different resolutions in QG and PE companion simulations. Spectral slopes close to -3 are observed in both KE and APE spectra down to scales corresponding to dx_{eff} at all resolutions.

2) GRID-SCALE ASPECT RATIO: dx/dz

We now explore the effect of vertical resolution on the numerical solutions. In QG simulations, KE spectra (Fig. 11) show small differences when varying vertical resolution. Similar small differences are apparent on

APE spectra (Fig. 12) between $128^2 \times 60$ and $128^2 \times 120$, or between $256^2 \times 120$ and $256^2 \times 240$ grid configurations. However, APE spectra for $256^2 \times 240$ and $256^2 \times 480$ configurations are perfectly superimposed. Similarly in PE simulations, APE and APE dissipation spectra show slight differences between $512^2 \times 120$ and $512^2 \times 240$ grid configurations, while those of $512^2 \times 240$ and $512^2 \times 480$ configurations are superimposed. If we consider that a convergence of solutions is reached when spectra are perfectly superimposed, in terms of grid aspect ratio, QG simulations converge for $dx/dz \sim 2.8N/f$ ($dx_{\text{eff}}/dz \sim 9N/f$) and PE simulations converge for $dx/dz \sim 1.4N/f$ ($dx_{\text{eff}}/dz \sim 11N/f$). Note here that vertical dissipation also imposes some vertical effective resolution. The Splines scheme is nondissipative, but some dissipation is provided when combined with the time-stepping algorithm (Shchepetkin 2015). This small built-in

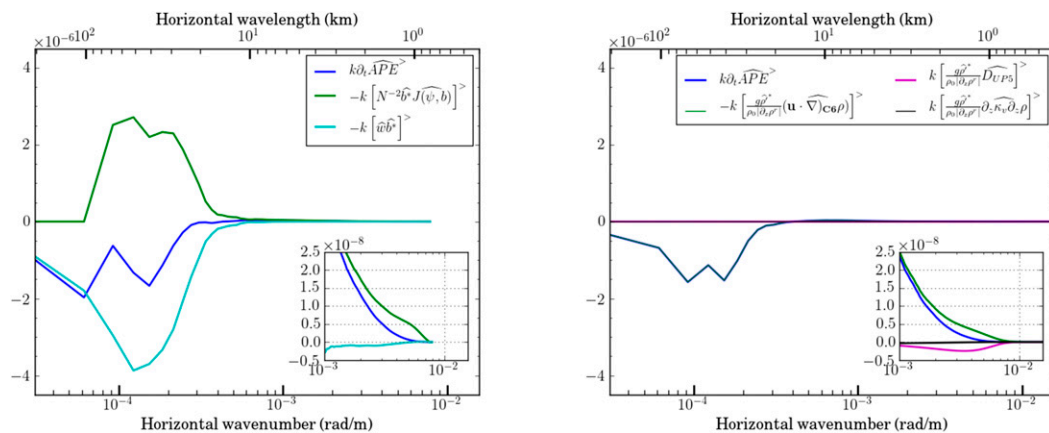


FIG. 10. APE budget (m s^{-3}) averaged between 80 and 120 days for (left) QG and (right) PE simulations. Terms are detailed in Eqs. (15) and (17). Note that dissipation is only significant at small scale in PE (no dissipation is applied on APE in the QG simulation).

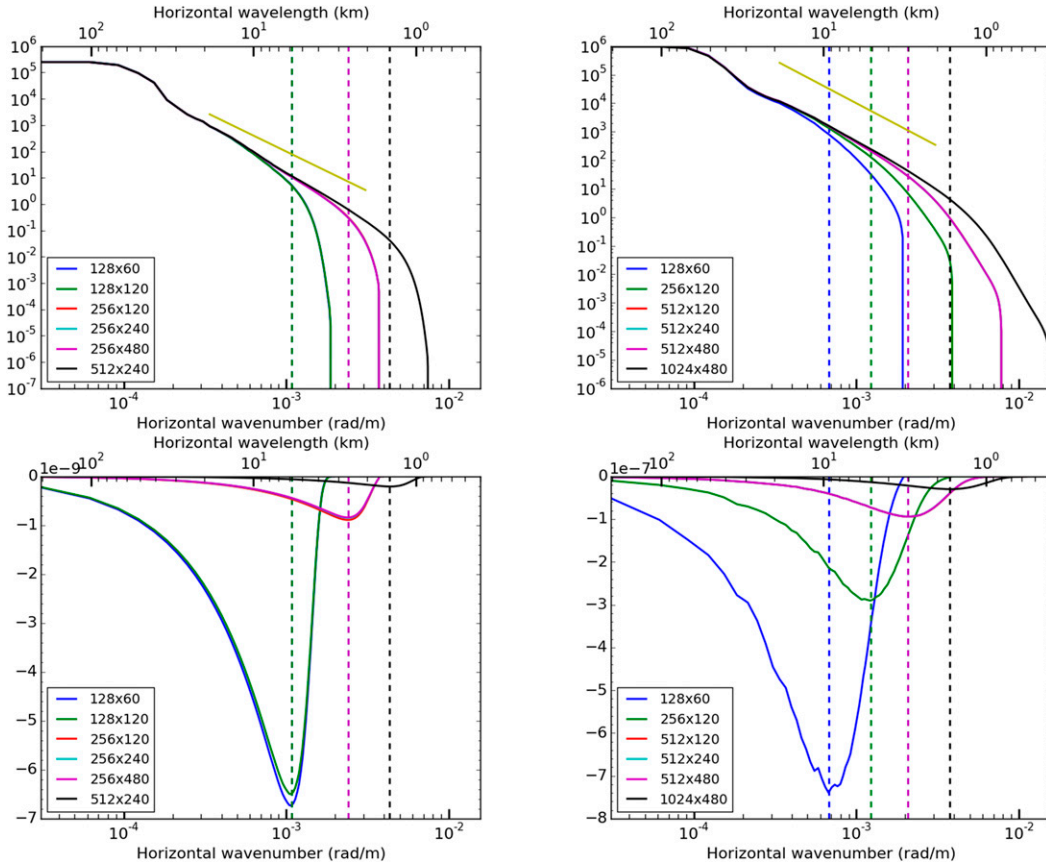


FIG. 11. (top) KE spectra ($m^3 s^{-2}$) averaged between 80 and 120 days at different resolutions with (bottom) their associated dissipation spectra ($m^3 s^{-2}$) for (left) QG and (right) PE simulations. Dissipation maxima are emphasized by vertical dashed lines. The yellow solid line is a -3 slope over one decade.

dissipation is in addition to the explicit Laplacian dissipation designed for physical closure. Spectral diagnostics are not straightforward for the vertical, but it would seem relevant to evaluate dz_{eff} and compare the ratio dx_{eff}/dz_{eff} to N/f . As an indication, considering that $dz_{eff} \geq 2dz$, dx_{eff}/dz would overestimate the value of dx_{eff}/dz_{eff} by at least a factor of 2. In any case, our converged solutions are close to the resolution requirement of $dx/dz = N/f$, beyond which, as pointed out in Lindzen and Fox-Rabinovitz (1989), Fox-Rabinovitz and Lindzen (1993), and Snyder et al. (1993) and mentioned in Nadiga (2014), spurious dynamics including spurious gravity wave activity can occur and provide incorrect numerical solutions.

3) EFFICIENCY OF A FORWARD ENERGY CASCADE

In Figs. 11 and 12, when resolution increases, dissipation decreases in magnitude and its scale range is shifted to smaller scales in both PE and QG simulations. However, in Molemaker et al. (2010), the reduction of dissipation with resolution is somewhat compensated by

the increase of forward energy cascade [spectral dissipation for a sixth-order operator varies as $k^6 KE(k)$]. In our PE experiment, the rapid fall of dissipation with resolution is indication that the forward cascade is less efficient and can hardly reach the dissipation range. Therefore, even though the formalism in this particular experiment is capable of forward cascade, the route to dissipation has only limited efficiency probably because of the absence of secondary instabilities at submesoscale.

b. Sensitivity to numerical settings in PE

1) HORIZONTAL ADVECTION SCHEMES: UP3 VS UP5

In PE simulations, special care was given to the representation of dissipation scales. Those are dependent on the order of accuracy of upwind advection schemes (UP3 or UP5). In Fig. 13, UP3 and UP5 schemes (third- or fifth-order accurate) for momentum and tracer equations are compared using KE and APE spectra and

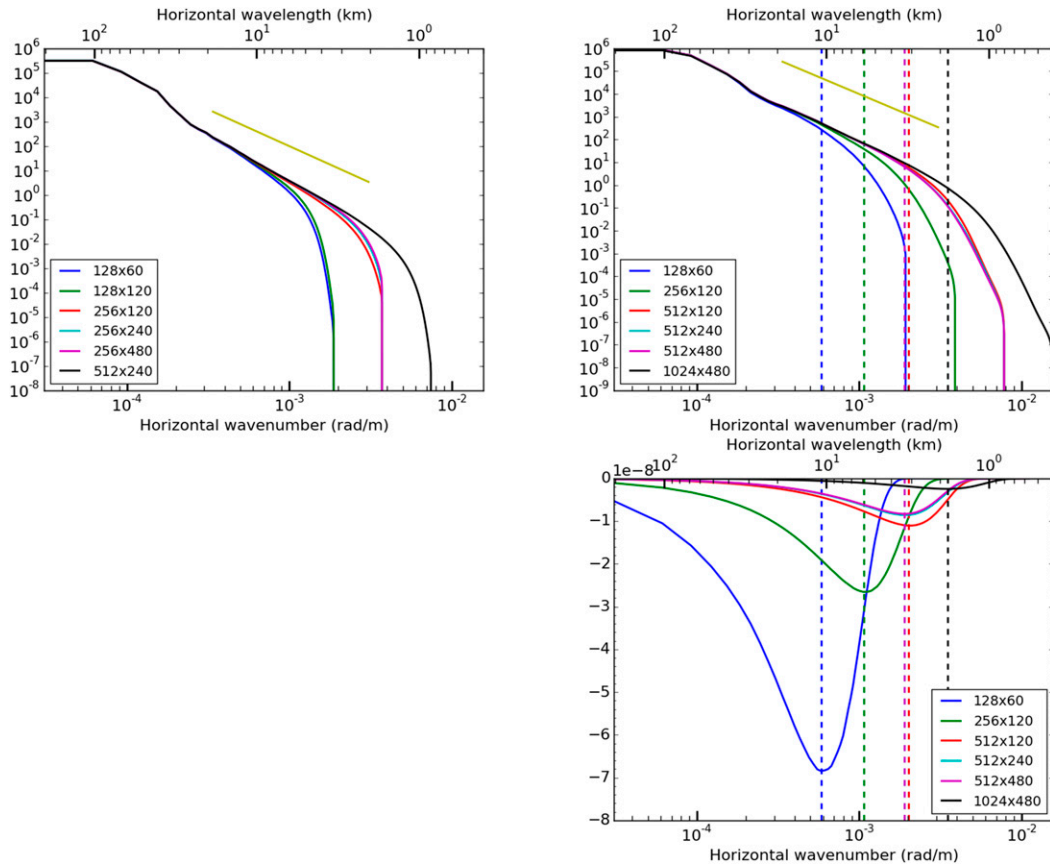


FIG. 12. (top) APE spectra ($\text{m}^3 \text{s}^{-2}$) averaged between 80 and 120 days at different resolutions for (top left) QG and (top right) PE simulations with (bottom right) their associated dissipation spectra ($\text{m}^2 \text{s}^{-3}$) in the PE simulations. Dissipation maxima are emphasized by vertical dashed lines. The yellow solid line is a -3 slope over one decade. Note the absence of dissipation in the QG APE budget [Eq. (15)].

associated dissipation terms. UP3 dissipation spectra have much larger amplitudes than UP5 and spread over a much broader range of scales. Actually, UP3 dissipation spectra at a given grid resolution are close to the equivalent UP5 spectra at twice-coarser resolution (and even broader). Correspondingly, KE and APE spectra fall earlier from their inertial range slope when using UP3. This comparison thus indicates that using a fifth-order rather than third-order accurate upstream scheme is equivalent to increasing the grid resolution by a factor of 2. This is a very efficient increase of effective resolution since the cost increase is only 6%.

2) VERTICAL TRACER ADVECTION SCHEMES: AKIMA VS SPLINES

The vertical tracer advection scheme is also critical to our simulations. The so-called Akima scheme (a fourth-order centered scheme with harmonic averaging; see Soufflet et al. 2016) is frequently used in ROMS-family codes for vertical tracer advection. In the present study, we use Splines, a fourth-order compact scheme with

much lower dispersion errors (i.e., the leading-order truncation term is many times smaller than that of conventional fourth-order schemes), which are overcome by the built-in dissipation of the time stepping scheme (Shchepetkin 2015). To explore the sensitivity of our results to vertical advection, Akima was tested, and Figs. 14 and 15 show its impact on the solutions with low and high vertical resolution. Horizontal energy spectra are significantly shallower at low vertical resolution and dissipation is substantially enhanced. The left column of Fig. 15 shows horizontal sections at vortex middepth of a tracer field for low and high vertical resolution with Akima and medium resolution with Splines. There is large production of small horizontal scales using Akima at low vertical resolution. This spurious energy production has great impact on the physical solution and the spectral distribution of energies (note the increase of horizontal dissipation with resolution as small-scale energy production is increased). Spurious submesoscale energy is produced because Akima has no implicit vertical diffusion. Although its dispersion

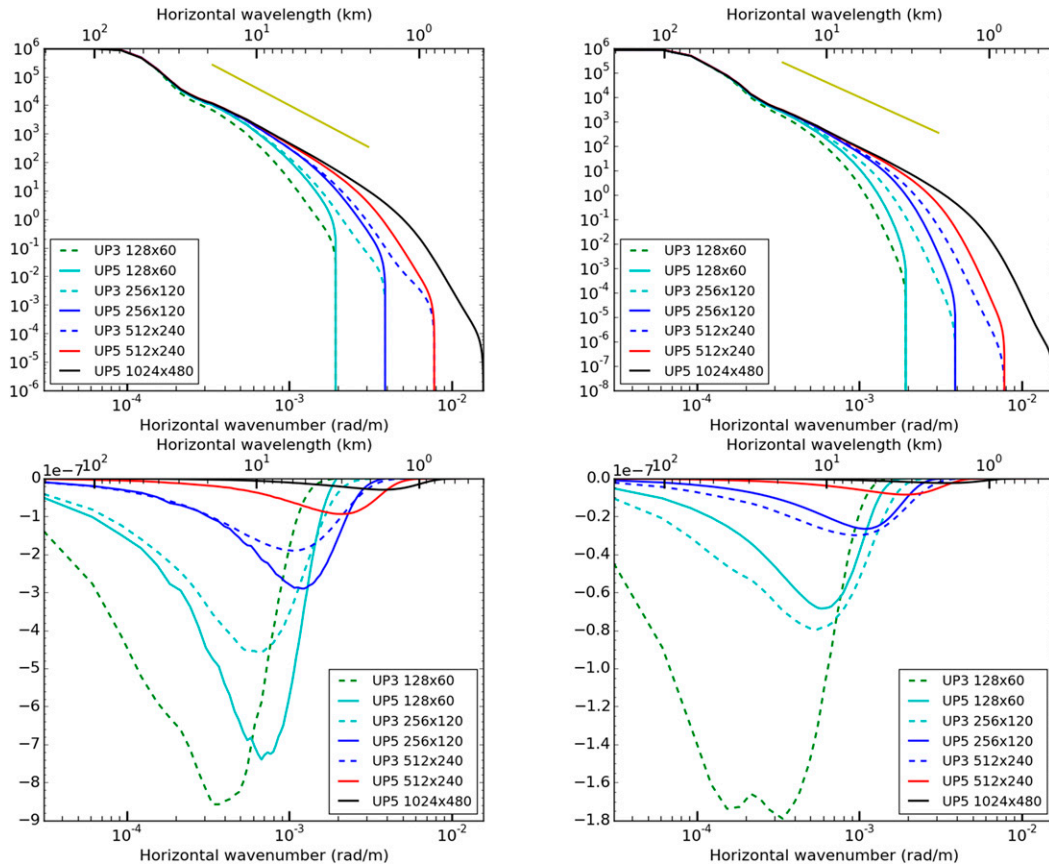


FIG. 13. (top left) KE and (top right) APE spectra ($\text{m}^3 \text{s}^{-2}$) averaged between 80 and 120 days in PE simulations for UP3 vs UP5 horizontal advection schemes (for both tracers and momentum) at different resolutions and with (bottom) their associated dissipation spectra ($\text{m}^2 \text{s}^{-3}$). The yellow solid line is a -3 slope over one decade.

errors are somewhat weaker than that produced by a more conventional fourth-order centered scheme with arithmetic averaging (C4), it still produces significant dispersion that is not attenuated by explicit vertical dissipation (even when multiplying diffusivity by 10, i.e., $10^{-5} \text{m}^2 \text{s}^{-1}$) or by implicit dissipation in the stepping scheme. The right column of Fig. 15 shows Ertel PV vertical sections inside the vortex. At low vertical resolution, we observe noise in the Ertel PV field, which can be associated with Akima's dispersion errors. This noise induces inversion of the isopycnal radial gradient of PV, which is a cause of baroclinic instability (Eliassen 1983). Increasing resolution significantly reduces the noise and the solution approaches that of a much less dispersive vertical advection scheme (Splines).

6. Discussion

We have studied spindown simulations of an unstable vortex to a mixed baroclinic–barotropic instability. Even though the global energy is almost conserved, a small amount (KE and APE) leaks down to dissipation

scales during the instability development. In our parameter regime, PE simulations do not show a substantial forward energy cascade sustained by unbalanced dynamics.

In this study, we did not question the relevance of the parameter regime (e.g., N/f or the Rossby number), but we clarified some numerical issues as they are detrimental to the physical solutions and confuse our interpretation of small-scale dynamics. Special care was given to determining the effective resolution of our simulations. In the spectral QG model, the smallest well-resolved horizontal scale is a bit more than 3 times the grid scale, while in the PE model, it is a bit less than 8 times. The difference can be associated with the order of horizontal dissipation operators in the QG and PE models (12 and 6, respectively). We improved by a factor of 2 the effective resolution of the PE finite-difference model (CROCO) by implementing a fifth-order accurate horizontal advection scheme (UP5) instead of the standard third-order scheme of ROMS-family codes, with only a 6% cost increase. We also explored different grid aspect ratios dx/dz and found

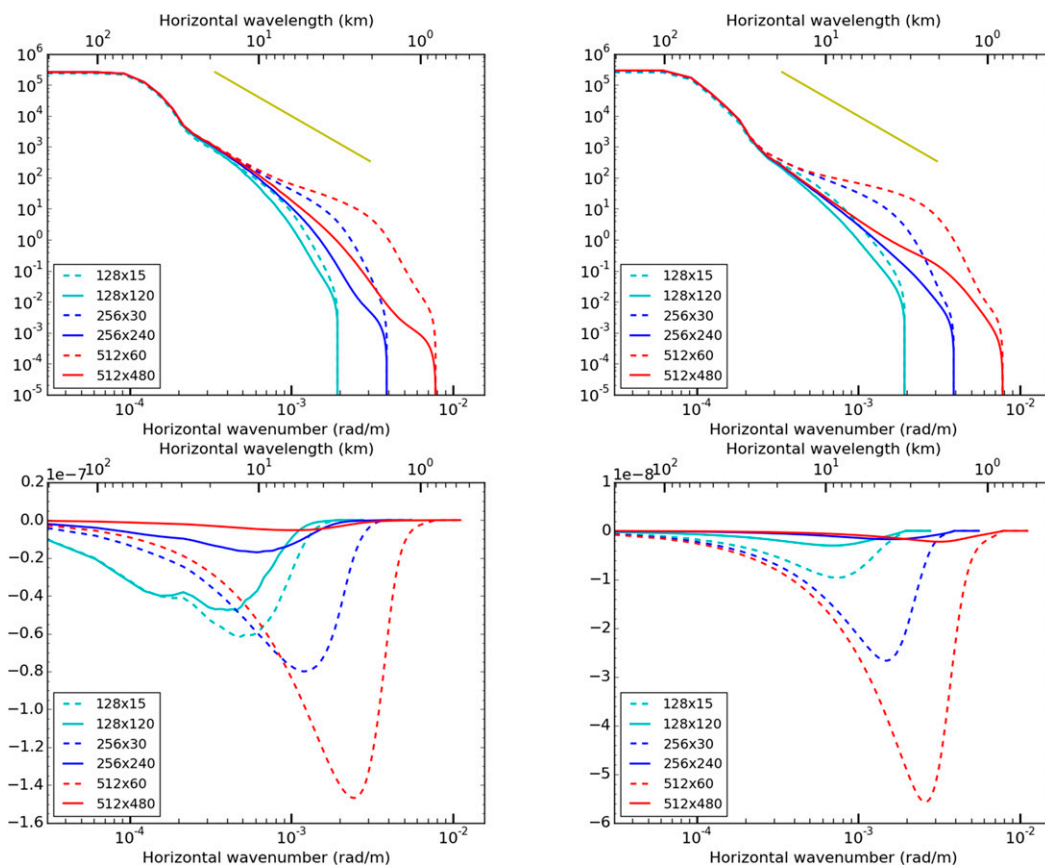


FIG. 14. (top left) KE and (top right) APE spectra ($\text{m}^3 \text{s}^{-2}$) averaged between 80 and 120 days in PE simulations using the Akima vertical tracer advection scheme for different grid aspect ratio and at different resolutions, along with (bottom) their associated dissipation spectra ($\text{m}^2 \text{s}^{-3}$). The yellow solid line is a -3 slope over one decade.

that our energy spectra and spectral fluxes converge for aspect ratios that are close to N/f in both QG and PE models.

However, this convergence is not reached in the PE model when the Akima vertical advection scheme is used for tracers. This dispersive scheme used with small vertical diffusivity generates noise on the vertical grid, which sustains baroclinic instabilities in our simulations and generates submesoscale horizontal features. This spurious secondary instability has great impact on the production of finescale dynamics and the energy cascade. Therefore, the experiment underlines the importance of numerical errors produced by vertical advection schemes, which are often overlooked compared with horizontal advection. It also illustrates how spurious mechanisms can generate submesoscale energy in similar fashion as physical instabilities. It thus emphasizes the risk of using centered numerical schemes with suboptimal filtering in the hope of increasing effective resolution. For vertical fluxes, the problem is

particularly critical as modelers generally attempt to reduce diapycnal mixing in order to preserve water-mass structures and isopycnal slopes. Our results confirm that reduction of mixing can only be achieved with accurate numerical methods.

The present choice of numerical setting (including the implementation of a fifth-order horizontal advection scheme) appears well fitted to our physical problem. Increasing vertical turbulent viscosity and diffusivity brings considerable smoothing to the layer structures around the meddy. This indicates that the physical problem is now better controlled by physical closure rather than numerical errors. It was not the case, for example, with standard third-order horizontal advection. The choice of a finite-difference PE model (rather than pseudospectral) was dictated by the need to study oceanic scale interaction problems in progressively more realistic applications. The present study can be considered as an evaluation of model numerics in anticipation of such applications.

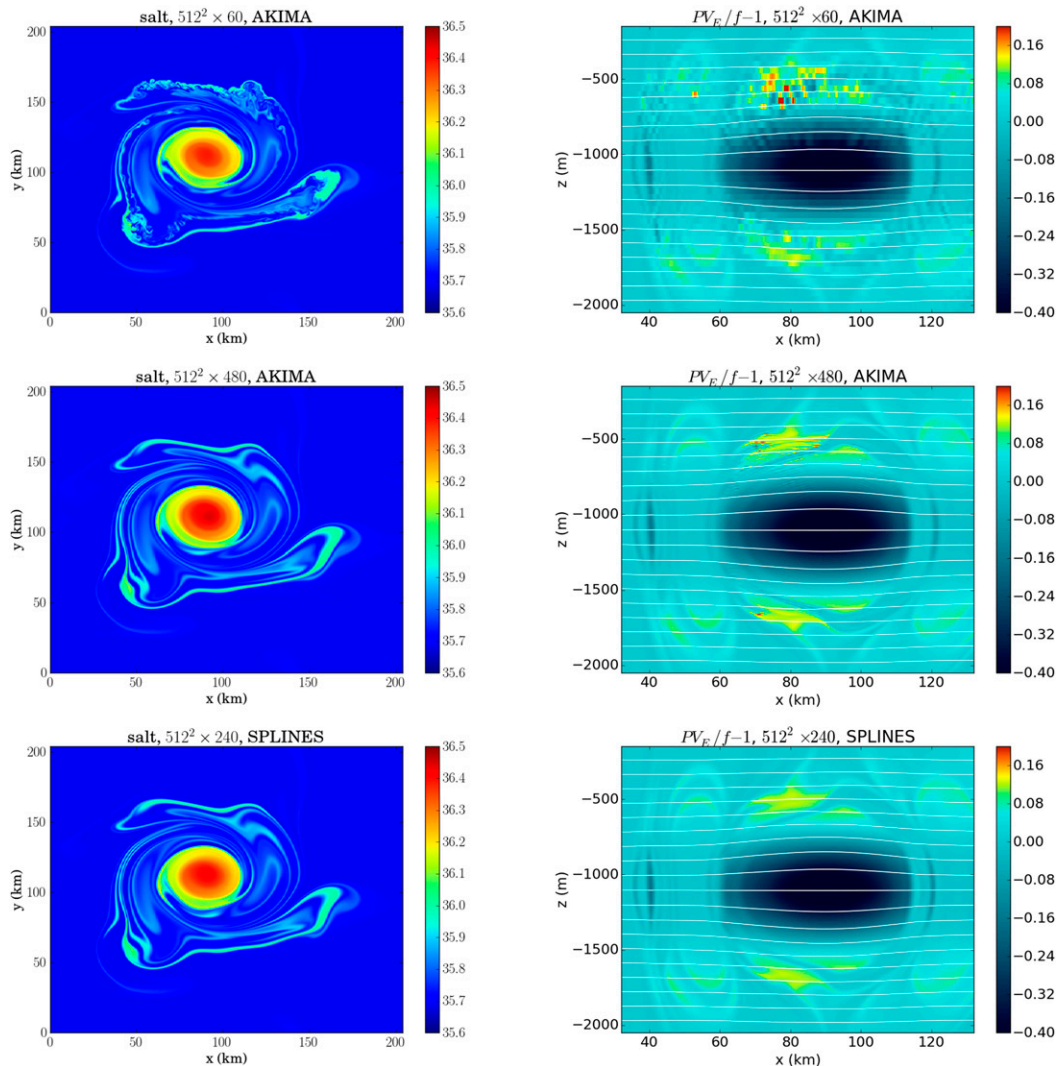


FIG. 15. (left) Horizontal sections of salt at 1420 m and (right) vertical sections of $(PV_E/f - 1)$ across the vortex core for PE simulations. (top) The 512×60 grid configuration using the Akima vertical tracer advection scheme. (middle) The 512×480 grid configuration using Akima. (bottom) The 512×240 grid configuration using the Splines vertical tracer advection scheme.

The study of direct submesoscale energy cascade in the ocean interior is at the limit of PE model capability. For example, the grid aspect ratio has to be revisited in order to consistently address nonhydrostatic effects, which should be evaluated. Parameter regimes also need to be explored. In particular, as noted by Capet et al. (2016), the N/f ratio is rather small in all studies that have found a significant forward energy flux at small scale. On the other hand, increasing the Rossby number should boost unbalanced dynamics, which can sustain secondary instabilities at small scale and thus a forward energy flux. In our study, we did not address the efficiency of the interior route to dissipation associated with processes other than instabilities sustained by the

mesoscale activity. Inertial waves, for example, can also stimulate imbalance and enhance eddy kinetic energy dissipation (Barkan et al. 2017). Interactions between interior mesoscale activity and internal waves should also be accounted for.

Acknowledgments. We thank Florian Lemarié and Xavier Capet for helpful discussions. We thank reviewers for their help in clarifying the manuscript. We acknowledge the support of LabexMER-Axe1 and GENCI Research Infrastructure through Allocation A0010106130. We acknowledge the support of LEFE/IMAGO through the Project AO2017-994457-RADII.

REFERENCES

- Armi, L., D. Hebert, N. Oakey, J. F. Price, P. L. Richardson, H. T. Rossby, and B. Ruddick, 1989: Two years in the life of a Mediterranean salt lens. *J. Phys. Oceanogr.*, **19**, 354–370, [https://doi.org/10.1175/1520-0485\(1989\)019<0354:TYITLO>2.0.CO;2](https://doi.org/10.1175/1520-0485(1989)019<0354:TYITLO>2.0.CO;2).
- Barkan, R., K. B. Winters, and J. C. McWilliams, 2017: Stimulated imbalance and the enhancement of eddy kinetic energy dissipation by internal waves. *J. Phys. Oceanogr.*, **47**, 181–198, <https://doi.org/10.1175/JPO-D-16-0117.1>.
- Bartello, P., 1995: Geostrophic adjustment and inverse cascades in rotating stratified turbulence. *J. Atmos. Sci.*, **52**, 4410–4428, [https://doi.org/10.1175/1520-0469\(1995\)052<4410:GAAICT>2.0.CO;2](https://doi.org/10.1175/1520-0469(1995)052<4410:GAAICT>2.0.CO;2).
- Biescas, B., V. Sallarès, J. L. Pelegrí, F. Machín, R. Carbonell, G. Buffett, J. J. Dañobeitia, and A. Calahorrano, 2008: Imaging meddy fine-structure using multichannel seismic reflection data. *Geophys. Res. Lett.*, **35**, L11609, <https://doi.org/10.1029/2008GL033971>.
- Brüggemann, N., and C. Eden, 2015: Routes to dissipation under different dynamical conditions. *J. Phys. Oceanogr.*, **45**, 2149–2168, <https://doi.org/10.1175/JPO-D-14-0205.1>.
- Capet, X., G. Roullet, P. Klein, and G. Maze, 2016: Intensification of upper-ocean submesoscale turbulence through Charney baroclinic instability. *J. Phys. Oceanogr.*, **46**, 3365–3384, <https://doi.org/10.1175/JPO-D-16-0050.1>.
- Debreu, L., P. Marchesiello, P. Penven, and G. Cambon, 2012: Two-way nesting in split-explicit ocean models: Algorithms, implementation and validation. *Ocean Modell.*, **49–50**, 1–21, <https://doi.org/10.1016/j.ocemod.2012.03.003>.
- Demange, J., L. Debreu, P. Marchesiello, F. Lemarié, and E. Blayo, 2014: On the use of a depth-dependent barotropic mode in ocean models: Impact on the stability of the coupled barotropic/baroclinic system. INRIA Tech. Rep. RR-8589, 31 pp.
- Durran, D. R., 2010: *Numerical Methods for Fluid Dynamics: With Applications to Geophysics*. Texts in Applied Mathematics, Vol. 32, Springer, 516 pp.
- Eliassen, A., 1983: The Charney-Stern theorem on barotropic-baroclinic instability. *Pure Appl. Geophys.*, **121**, 563–572, <https://doi.org/10.1007/BF02590155>.
- Fox-Rabinovitz, M. S., and R. S. Lindzen, 1993: Numerical experiments on consistent horizontal and vertical resolution for atmospheric models and observing systems. *Mon. Wea. Rev.*, **121**, 264–271, [https://doi.org/10.1175/1520-0493\(1993\)121<0264:NEOCHA>2.0.CO;2](https://doi.org/10.1175/1520-0493(1993)121<0264:NEOCHA>2.0.CO;2).
- Frisch, U., 1995: *Turbulence*. Cambridge University Press, 296 pp.
- Hoskins, B. J., I. Draghici, and H. C. Davies, 1978: A new look at the ω -equation. *Quart. J. Roy. Meteor. Soc.*, **104**, 31–38, <https://doi.org/10.1002/qj.49710443903>.
- Hua, B. L., and D. B. Haidvogel, 1986: Numerical simulations of the vertical structure of quasi-geostrophic turbulence. *J. Atmos. Sci.*, **43**, 2923–2936, [https://doi.org/10.1175/1520-0469\(1986\)043<2923:NSOTVS>2.0.CO;2](https://doi.org/10.1175/1520-0469(1986)043<2923:NSOTVS>2.0.CO;2).
- , C. Ménesguen, S. Le Gentil, R. Schopp, B. Marsset, and H. Aiki, 2013: Layering and turbulence surrounding an anticyclonic oceanic vortex: In situ observations and quasi-geostrophic numerical simulations. *J. Fluid Mech.*, **731**, 418–442, <https://doi.org/10.1017/jfm.2013.369>.
- Large, W. G., J. C. McWilliams, and S. C. Doney, 1994: Oceanic vertical mixing: A review and a model with a nonlocal boundary layer parameterization. *Rev. Geophys.*, **32**, 363–403, <https://doi.org/10.1029/94RG01872>.
- Lindzen, R. S., and M. Fox-Rabinovitz, 1989: Consistent vertical and horizontal resolution. *Mon. Wea. Rev.*, **117**, 2575–2583, [https://doi.org/10.1175/1520-0493\(1989\)117<2575:CVAHR>2.0.CO;2](https://doi.org/10.1175/1520-0493(1989)117<2575:CVAHR>2.0.CO;2).
- Marchesiello, P., X. Capet, C. Menkes, and S. C. Kennan, 2011: Submesoscale dynamics in tropical instability waves. *Ocean Modell.*, **39**, 31–46, <https://doi.org/10.1016/j.ocemod.2011.04.011>.
- Marino, R., A. Pouquet, and D. Rosenberg, 2015: Resolving the paradox of oceanic large-scale balance and small-scale mixing. *Phys. Rev. Lett.*, **114**, 114504, <https://doi.org/10.1103/PhysRevLett.114.114504>.
- Ménesguen, C., B.-L. Hua, X. Carton, F. Klingelhoefer, P. Schnürle, and C. Reichert, 2012: Arms winding around a meddy seen in seismic reflection data close to the Morocco coastline. *Geophys. Res. Lett.*, **39**, L05604, <https://doi.org/10.1029/2011GL050798>.
- Meunier, T., C. Ménesguen, R. Schopp, and S. Le Gentil, 2015: Tracer stirring around a meddy: The formation of layering. *J. Phys. Oceanogr.*, **45**, 407–423, <https://doi.org/10.1175/JPO-D-14-0061.1>.
- Molemaker, M. J., J. C. McWilliams, and X. Capet, 2010: Balanced and unbalanced routes to dissipation in an equilibrated Eady flow. *J. Fluid Mech.*, **654**, 35–63, <https://doi.org/10.1017/S0022112009993272>.
- Nadiga, B. T., 2014: Nonlinear evolution of a baroclinic wave and imbalanced dissipation. *J. Fluid Mech.*, **756**, 965–1006, <https://doi.org/10.1017/jfm.2014.464>.
- Nandi, P., W. S. Holbrook, S. Pearse, P. Páramo, and R. W. Schmitt, 2004: Seismic reflection imaging of water mass boundaries in the Norwegian Sea. *Geophys. Res. Lett.*, **31**, L23311, <https://doi.org/10.1029/2004GL021325>.
- Nguyen, H. Y., B. L. Hua, R. Schopp, and X. Carton, 2012: Slow quasigeostrophic unstable modes of a lens vortex in a continuously stratified flow. *Geophys. Astrophys. Fluid Dyn.*, **106**, 305–319, <https://doi.org/10.1080/03091929.2011.620568>.
- Pedlosky, J., 1996: *Ocean Circulation Theory*. Springer, 456 pp.
- Pouquet, A., and R. Marino, 2013: Geophysical turbulence and the duality of the energy flow across scales. *Phys. Rev. Lett.*, **111**, 234501, <https://doi.org/10.1103/PhysRevLett.111.234501>.
- Shchepetkin, A. F., 2015: An adaptive, courant-number-dependent implicit scheme for vertical advection in oceanic modeling. *Ocean Modell.*, **91**, 38–69, <https://doi.org/10.1016/j.ocemod.2015.03.006>.
- , and J. C. McWilliams, 2005: The Regional Oceanic Modeling System (ROMS): A split-explicit, free-surface, topography-following-coordinate oceanic model. *Ocean Modell.*, **9**, 347–404, <https://doi.org/10.1016/j.ocemod.2004.08.002>.
- Snyder, C., W. C. Skamarock, and R. Rotunno, 1993: Frontal dynamics near and following frontal collapse. *J. Atmos. Sci.*, **50**, 3194–3212, [https://doi.org/10.1175/1520-0469\(1993\)050<3194:FDNAFF>2.0.CO;2](https://doi.org/10.1175/1520-0469(1993)050<3194:FDNAFF>2.0.CO;2).
- Song, H., L. M. Pinheiro, B. Ruddick, and F. C. Teixeira, 2011: Meddy, spiral arms, and mixing mechanisms viewed by seismic imaging in the Tagus abyssal plain (SW Iberia). *J. Mar. Res.*, **69**, 827–842, <https://doi.org/10.1357/002224011799849309>.
- Soufflet, Y., P. Marchesiello, F. Lemarié, J. Jouanno, X. Capet, L. Debreu, and R. Benshila, 2016: On effective resolution in ocean models. *Ocean Modell.*, **98**, 36–50, <https://doi.org/10.1016/j.ocemod.2015.12.004>.
- Storer, B. A., F. J. Poulin, and C. Ménesguen, 2018: The dynamics of quasigeostrophic lens-shaped vortices. *J. Phys. Oceanogr.*, **48**, 937–957, <https://doi.org/10.1175/JPO-D-17-0039.1>.
- Yim, E., P. Billant, and C. Ménesguen, 2016: Stability of an isolated pancake vortex in continuously stratified-rotating fluids. *J. Fluid Mech.*, **801**, 508–553, <https://doi.org/10.1017/jfm.2016.402>.